

Measurements of the Atmospheric Mass, Energy, and Momentum Budgets Over a 500-Kilometer Square of Tropical Ocean

JOSHUA Z. HOLLAND and EUGENE M. RASMUSSEN—Center for Experiment Design and Data Analysis, Environmental Data Service, NOAA, Washington, D.C.

ABSTRACT—The atmospheric budgets of mass, water vapor, heat, momentum, and mechanical energy have been analyzed for a 5-day undisturbed period (June 22–26, 1969) during the Barbados Oceanographic and Meteorological Experiment (BOMEX). Data were obtained from rawinsondes launched every 1½ hr from the four corner ships of the BOMEX array. Computations were limited to the lowest 500 mb within a 500-km square centered at 15°N, 56°30'W. The mass budget is characterized by mean, low-level divergence and downward motion. Maximum divergence ($5 \times 10^{-6} \text{ s}^{-1}$) is found approximately 80 mb above the surface and maximum subsidence near the base of the trade-wind inversion. The computed average evaporation is 6.0 mm/day. The computations show an upward flux of moisture through the trade in-

version by subgrid-scale eddies, but the mean downward flux dominates, leading to a net downward transfer of moisture through the trade inversion. A surface stress of 0.065 Newtons (N)·m⁻² is computed from the momentum balance with the top of the friction layer approximately 130 mb above the surface. Computed frictional loss of grid-scale kinetic energy within the boundary layer is 0.8 W·m⁻². Heat balance computations indicate a Bowen ratio of approximately 0.1. Comparison of profiles of subgrid-scale moisture flux and nonradiative diabatic heating suggests that condensation and evaporation processes associated with the development and dissipation of trade-wind cumulus can make a significant contribution to the heat balance of the cloud and trade inversion layers.

1. INTRODUCTION

The primary objective of the Sea-Air Interaction Program, or "Core Experiment," of the Barbados Oceanographic and Meteorological Experiment (BOMEX) was to determine the rate of transfer of water vapor, heat, and momentum from the tropical ocean to the atmosphere. The 500-km square ship array represented the grid spacing proposed for future global observation networks. Data were to be obtained over a time period sufficient for observation of typical day-to-day variations associated with synoptic scale phenomena and with a time and space resolution sufficient for an evaluation of the relative magnitudes of grid-scale and subgrid-scale transport processes.

The experiment, designed by Davidson (1968), was conducted during May and June 1969 over the area east of Barbados (fig. 1). The season was chosen to provide a wide range of convective activity without well-developed storms. The observational program is described by the Barbados Oceanographic and Meteorological Analysis Project (BOMAP Office 1971).

In continuing analyses of the Core Experiment, independent estimates of the sea-air fluxes of heat, water vapor, and momentum are being made, based on oceanographic, micrometeorological, and grid-scale meteorological data. Preliminary results of the analyses of the BOMEX oceanographic and micrometeorological data have been summarized by Delnore (1972) and Holland (1972). The synoptic-scale data include those collected by the ships in the 500-km array, by aircraft flying around the perimeter

of the array, and by dropsondes released on a pattern inside the array, supplemented by radiometersonde, radar, and satellite observations.

This paper deals with a trial analysis of the atmospheric budgets of mass, water vapor, heat, momentum, and mechanical energy based on preliminary rawinsonde data from the four corner ships.

2. DATA BASE

A 5-day period of intensive rawinsonde observations was selected for the trial budget computations. This period, June 22–26, 1969, was marked by relatively undisturbed trade-wind weather. The rawinsonde program developed by Davidson (1968) called for 15 soundings per day during intensive periods, with a surface meteorological observation at each balloon launch time. It was hoped that, by averaging to an acceptable level, this number would permit random errors in humidity and wind velocity derivatives to be reduced for computation of the water vapor budget terms (Holland 1970).

The soundings were made with separate temperature and humidity sondes, each with its own transmitter. The temperature sensors were thermistors that had been individually calibrated in the factory and selected for minimum error. A special midreference frequency was transmitted by the temperature sonde for more accurate calibration. The humidity sensors were hygristors that had been batch calibrated. The temperature, humidity, and reference audio frequency signals, as well as the slant range and coarse and fine azimuth measured by a Scanwell

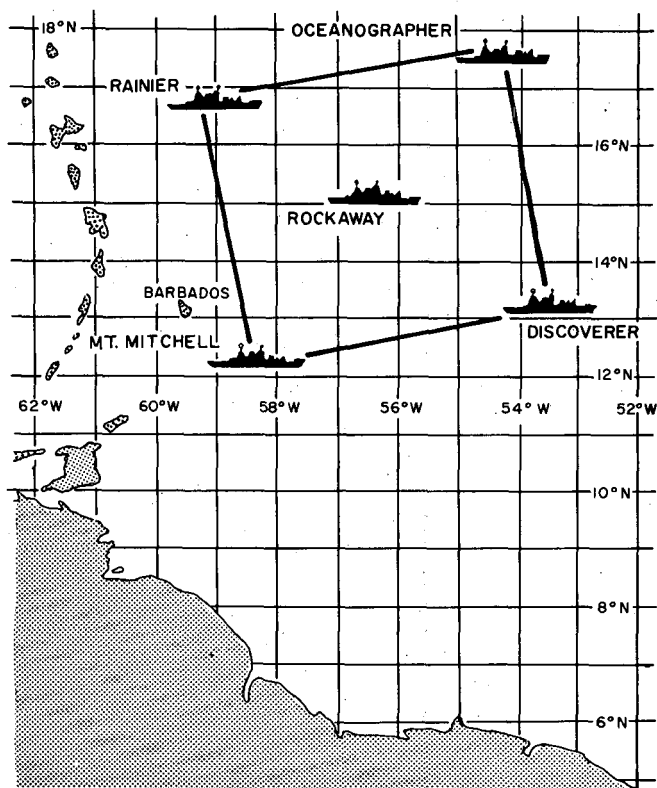


FIGURE 1.—Ship array during BOMEX Observation Periods I, II, and III, May 1–July 1, 1969.

Wind Finding at Sea system,¹ were recorded on magnetic tape in analog form by a NASA Signal Conditioning and Recording Device (SCARD) on three of the corner ships (*Mt. Mitchell*, *Oceanographer*, and *Rainier*). The fourth ship (*Discoverer*) had the same recording system but used a Selenia radar for balloon tracking with separate recording of azimuth and slant range.

After the field phase, the analog tapes were digitized and the data reduced by a preliminary “A₀” process at the NASA Mississippi Test Facility. A final “A” data reduction process is underway, following an exhaustive study of the A₀ data. The large yield of usable rawinsonde data from the A₀ process has encouraged us to carry out the computations discussed here with these data.

The rawinsonde schedule during the 5-day period called for flights at 0000 GMT until the balloon burst and flights to 400 mb at 1½-hr intervals between 0300 and 2230 GMT. A number of the scheduled flights were, however, missed or not processed by the A₀ program. Most prominent among the missing data are the 0000 GMT ascents by the *Rainier* and *Discoverer*, which were not incorporated into the data base because of problems that arose in the automatic evaluation of the radiometersonde data transmitted along with the usual data by these sondes. Also, because of a particular shortage of data early on the 22d and late on the 26th, the budgets were actually computed for slightly less than 5 days (0300 GMT on June 22–2100 GMT on June 26). A significant

fraction of the soundings reached 500 mb but failed to reach 400 mb.

Computations were made at intervals of 10 mb from the surface to 500 mb above the surface. A p^* -coordinate system was used, where p^* is the position on the vertical axis in terms of pressure differential relative to sea level; that is, $p^*=0$ at sea level and 500 mb at the top of the BOMEX “box” (Rasmusson 1971a). Basic observed variables used in the computations are the eastward wind component, u , the northward component, v , specific humidity, q , and temperature, T .

Before the budget computations were carried out, the basic data at each level were examined, and any values more than three standard deviations from the mean at that level were discarded. Next, missing values were filled in by fitting a cubic spline function to the data points at each level. This resulted in a set of values for each basic parameter (u , v , T , q) every 1½ hr. Finally, the data for each level were filtered to remove all fluctuations with periods less than 6 hr. Fluctuations having periods 12 hr or more were passed unattenuated.

The handling of the humidity data presented a special problem, due to errors arising from temperature lag and heating of the hygistor caused by radiation. The radiation error occurs in the data obtained during daylight hours and induces a spurious diurnal variation in the humidity values (Teweles 1970). As a preliminary expedient to minimize the effect of the radiation error, the mean “observed” diurnal variation was removed from the data by adding to the individual hourly value the difference between the mean value at that hour and the mean value at the hour of maximum specific humidity. The adjustment is based on the assumption that the maximum specific humidity values, which are observed during the nighttime hours, are correct.

The various budget terms have been computed for each 1½-hr observation time during the 5-day period, but only the mean budgets for the period under investigation will be discussed.

3. ATMOSPHERIC CIRCULATION FEATURES

Conditions during the 5-day period were undisturbed. Analyses based on satellite data and radar observations from the *Discoverer* and the island of Barbados indicated an average value of precipitation of only 0.2 mm/day with relatively small day-to-day variations.

Average values of u , v , T , and q as functions of p^* are illustrated in figure 2. Both the observed and corrected values of dew point are shown. The mean temperature lapse rate was dry adiabatic through the first 50 mb. The most stable layer was found between $p^*=170$ mb and $p^*=210$ mb. An actual inversion, such as appears on many individual soundings, was not found on the mean sounding due to temporal and spatial variations in the height and intensity of the inversion. Above the trade inversion, the lapse rate is between dry and moist adiabatic, as noted by other investigators (e.g., Malkus 1962).

The low-level easterlies exhibited the typical trade-wind maximum 80 mb above the surface, then decreased

¹ Mention of a commercial product does not constitute an endorsement.

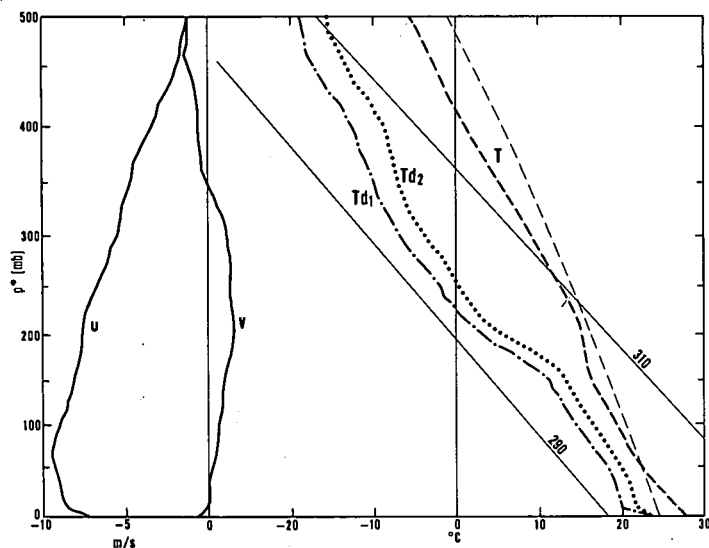


FIGURE 2.—Average vertical profiles of westerly wind component, u , southerly wind component, v , temperature, T , uncorrected dew-point temperature, Td_1 , and dew-point temperature, Td_2 , corrected for deviation from diurnal maximum, versus p^* . Dry adiabats for potential temperatures 290° and 310° K are shown for reference.

steadily. Winds at $p^*=500$ mb averaged light easterly, although observations from the *Oceanographer* exhibited light westerlies above $p^*=400$ mb. The average meridional wind component was small at all levels with a weak maximum around $p^*=210$ mb.

While atmospheric conditions within the BOMEX box during the period under investigation can be described as undisturbed, they cannot be characterized as steady, even after removal of diurnal variations. Particularly noteworthy were the variations in the winds and in the intensity and height of the trade inversion.

The variations in the intensity and height of the trade inversion are illustrated by the potential temperature cross-section for the *Oceanographer* (fig. 3). The zone of stability associated with the trade inversion was centered approximately on the 305° K isentrope at all four ships. Significant changes in the thermal structure took place during the middle of the period when the trade inversion rose and weakened markedly, accompanied by warming and downward propagation of a stable layer at higher levels. These thermal changes were also accompanied by sharp changes in humidity in the vicinity of the stable layers.

Day-to-day variations in the wind components were also significant above the trade inversion. Overall changes during the 5-day period ranged up to 19 m/s in the meridional component. Generally, the flow shifted to a more northwesterly direction during the first 4 days.

4. GENERALIZED BUDGET FORMULATION AND NOTATION

A generalized budget equation,² applicable to the data collection network being used, can be written in the

² Derivations of the budget equations in p^* coordinates have been discussed in detail by Rasmusson (1971a).

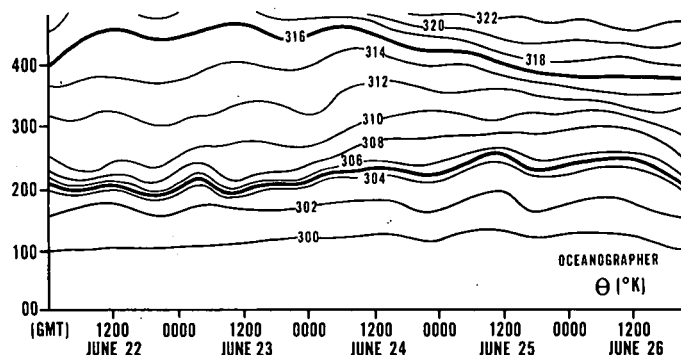


FIGURE 3.—Potential temperature time cross-section for the *Oceanographer*, June 22–26, 1969. Ordinate is p^* (mb).

following form:

$$\frac{d\bar{X}^A}{dt} = -g \frac{\partial \bar{D}_z^A}{\partial p^*} + \sum_{i=1}^N \bar{S}_i^A \quad (1)$$

where X is a generalized property per unit mass; $(\bar{\quad})^A$ is a grid-scale area average on a p^* surface; D_z is a generalized vertical diffusion term for the property, X , that includes the contribution to the vertical flux by all subgrid-scale eddies as well as the effect of molecular diffusion; and $\sum_{i=1}^N \bar{S}_i$ is the summation of all source and sink terms appearing in the balance equation for the property, X . Note that, in a broader context, these terms may also represent conversion terms, as, for example, conversion from liquid water to water vapor or conversion from one form of energy to another.

Expanding the substantial derivative, using the mass continuity equation, applying the Gauss theorem, and integrating between two p^* surfaces, p_B^* and p_T^* , we obtain

$$\frac{\partial}{\partial t} \int_{p_B^*}^{p_T^*} \bar{X}^A \frac{dp^*}{g} + \frac{C}{A} \int_{p_B^*}^{p_T^*} [\bar{X}^c \bar{V}_n^c + \bar{X}^{(c)} \bar{V}_n^{(c)}] \frac{dp^*}{g} + \frac{\bar{\omega}_T^A \bar{X}_T^A}{g} - \frac{\bar{\omega}_B^A \bar{X}_B^A}{g} = (\bar{D}_z^A)_B - (\bar{D}_z^A)_T + \sum_{i=1}^N \int_{p_B^*}^{p_T^*} \bar{S}_i^A \frac{dp^*}{g} \quad (2)$$

where C is the perimeter of the array; A is the area of the array; V_n is the normal wind component on the perimeter, positive outward;

$$(\bar{\quad})^c = \frac{1}{C} \oint_C (\quad) dC$$

is a line integral average;

$$(\quad)^{(c)} = (\quad) - (\bar{\quad})^c$$

is the deviation from a line integral average; and subscripts B and T denote the p^* surfaces at the bottom and top of the column.

The horizontal flux has been split exactly into two terms. The term $\bar{X}^c \bar{V}_n^c$ is referred to as the mean

TABLE 1.—Notation for vertical diffusion and source terms in the budget equations

Budget (X)	Diffusion term (D_x)	Source terms (S_i)
Mass (unity)	None	None
Water vapor (q)	D_q	$e - c$
Momentum x component (U)	$-\tau_x$	$f(V - V_g)$
Momentum y component (V)	$-\tau_y$	$-f(U - U_g)$
Kinetic energy (K) (grid scale)	None	$g\mathbf{V} \cdot \frac{\partial \mathbf{r}}{\partial p^*}$ $-(\mathbf{V} \cdot \nabla \phi + \alpha \mathbf{V} \cdot \nabla p_0)$
Heat (H)	D_H	\dot{Q}_{RAD} $L(c - e)$ \dot{Q}_F $\alpha \omega$

divergence term and is approximately equivalent to the term $\mathbf{X} \cdot \nabla \mathbf{V}$ averaged over the area. The term $\overline{\mathbf{X}^{(c)} \mathbf{V}_n^{(c)}}$, defined as

$$\overline{\mathbf{X}^{(c)} \mathbf{V}_n^{(c)}} = \overline{\mathbf{X} \mathbf{V}_n} - \overline{\mathbf{X}} \overline{\mathbf{V}_n},$$

is referred to as the horizontal advection term and is approximately equivalent to the area average of the term $\mathbf{V} \cdot \nabla \mathbf{X}$ under conditions dominated by a large-scale flow such as the trade-wind regime.

In the mass, water vapor, x component momentum, y component momentum, kinetic energy, and heat budgets, X is replaced by unity, q , U , V , K , and H , respectively. As used in the momentum budget analysis, U and V are the wind components in the positive x and y directions, respectively, where the x direction is that of the mean surface wind. The notation for the vertical diffusion and source terms of each budget are given in table 1, where τ is the subgrid-scale stress with components τ_x and τ_y in the positive x and y directions, respectively; \mathbf{V} is the horizontal wind vector with components U and V ; U_g and V_g are the corresponding components of the geostrophic wind \mathbf{V}_g ; e and c are the evaporation and condensation (per unit mass) within the atmosphere; \dot{Q}_{RAD} , $L(c - e)$, and \dot{Q}_F are the radiation, condensation, and frictional heating rates; α is the specific volume; ϕ is the geopotential; and $\omega = dp/dt = -\omega^* + \partial p_0/\partial t + \mathbf{V} \cdot \nabla p_0$ is the vertical velocity in ordinary pressure coordinates.

5. MASS BUDGET

The computed mean divergence and vertical motion profiles for the 5-day period are shown in figure 4. Maximum values of divergence (4.5 to $5.0 \times 10^{-6} \text{ s}^{-1}$) are found around $p^* = 80$ mb, the level of maximum wind. The level of zero divergence and maximum mean downward motion is found just below the base of the stable layer, at $p^* = 160$ mb. The average values of divergence computed for three aircraft line integral missions of 10 hr

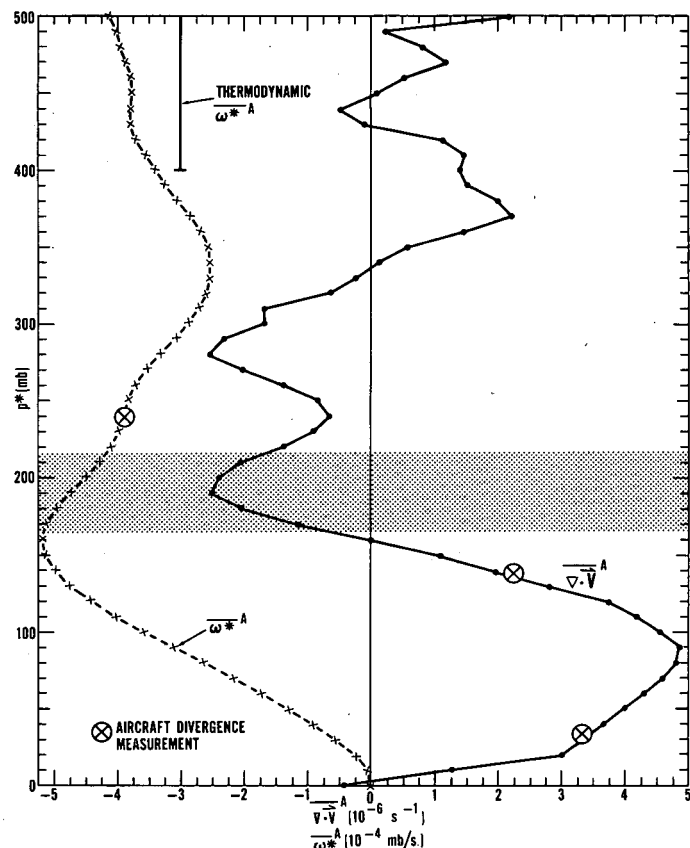


FIGURE 4.—Vertical profiles of horizontal velocity divergence from corner rawinsonde data, June 22–26, 1969, $\nabla \cdot \mathbf{V}^A$, and vertical velocity, $\omega^* A$, in p^* coordinates derived from the $\nabla \cdot \mathbf{V}^A$ profile. Circled Xs represent average horizontal divergence at 300-, 1300-, and 2300-m altitude from three aircraft missions. Also shown is the thermodynamic $\omega^* A$ computed from the heat budget of the 400- to 500-mb layer. The shaded area represents the p^* interval corresponding to the average trade inversion layer.

each on June 22 (day), June 23–24 (night), and June 25–26 (night) are also shown. Aircraft divergence values were obtained from the measured trend in the wind component parallel to the side of the box as well as the mean normal component, based on flights only along the eastern and western sides of the array (Holland 1971). The three-mission average divergence values can hardly be equated with the 5-day mean values obtained from the rawinsonde data. Nevertheless, the almost identical values obtained at the two levels below the trade inversion are encouraging. At the level above the trade inversion, where the flow is more variable, the values differ markedly.

As a check on the kinematically computed vertical velocity, we computed the vertical velocity in the upper layers of the box from the thermodynamic equation. During undisturbed conditions, the vertical velocity in the layers above the trade inversion is essentially that required to balance the effects of radiative cooling and horizontal heat advection; therefore, we have neglected the effect of subgrid-scale vertical heat transport and condensation heating in the computations. Values of radiative cooling were kindly provided by Stephen Cox of Colorado State University, Fort Collins, Colo.

TABLE 2.—Average water balance components

Component	Symbol	mm/day
Local change	$\frac{\partial}{\partial t} \int_0^{500} \bar{q}^A \frac{dp^*}{g}$	+0.5
Mean divergence	$\frac{C}{A} \int_0^{500} \bar{q}^C \bar{V}_n^C \frac{dp^*}{g}$	+5.7
Horizontal advection	$\frac{C}{A} \int_0^{500} \frac{\bar{q}^{(C)} \bar{V}_n^{(C)} dp^*}{g}$	+0.6
Flux through the top	$\frac{\bar{q}^A \omega^A}{g} 500$	-1.0
Precipitation	\bar{P}^A	+0.2
Evaporation	\bar{E}^A	6.0

Values for the thermodynamic ω^* should be most accurate near the top of the box, where the assumptions of zero condensation heating and subgrid-scale vertical heat transfer are most nearly satisfied. It is, therefore, encouraging to find that the difference between the kinematic and thermodynamic ω^* , averaged over the upper 100 mb of the box, is only 1×10^{-4} mb/s. In terms of the mean divergence of the column, the two values differ by approximately $2 \times 10^{-7} \text{ s}^{-1}$, or less than 20 percent, which represents satisfactory agreement. Standard deviations of the individual 1½-hr kinematic divergence values range from around 3 to $4 \times 10^{-6} \text{ s}^{-1}$ in the lowest 300 mb up to generally 6 to $8 \times 10^{-6} \text{ s}^{-1}$ in the upper portions of the box. Positive, low-level divergence is obtained at almost all observation times during the 5-day period. This is usually capped by a region of convergence as shown in figure 4. The divergence pattern computed for the upper half of the box is more variable and, at least during this 5-day period, exhibited a significant diurnal variation (Rasmusson 1971b).

6. WATER VAPOR BALANCE

Table 2 gives the average values for the individual terms of the water vapor budget, written with evaporation as the residual. Thus, the sign of each term is the sign of the evaporation increment required to balance it. An evaporation rate of $6.0 \text{ mm} \cdot \text{day}^{-2}$ was computed for the period. The mean divergence term is the major term in the balance equation. The horizontal advection term makes a relatively small contribution, amounting to only 10 percent of the mean flux divergence.

Profiles for the horizontal flux divergence terms are shown in figure 5. The mean divergence term below the trade inversion obviously constitutes the dominant contribution to the total flux divergence. In fact, the amount of water vapor transported from the box by the action of the low-level divergence during this period was roughly equal to the total evaporation.

Since average precipitation during the period is a negligible term in the vapor balance, the divergence of subgrid-scale vertical moisture flux can be evaluated as the residual of eq (1). We can then compute a profile of the subgrid-scale vertical moisture flux, beginning

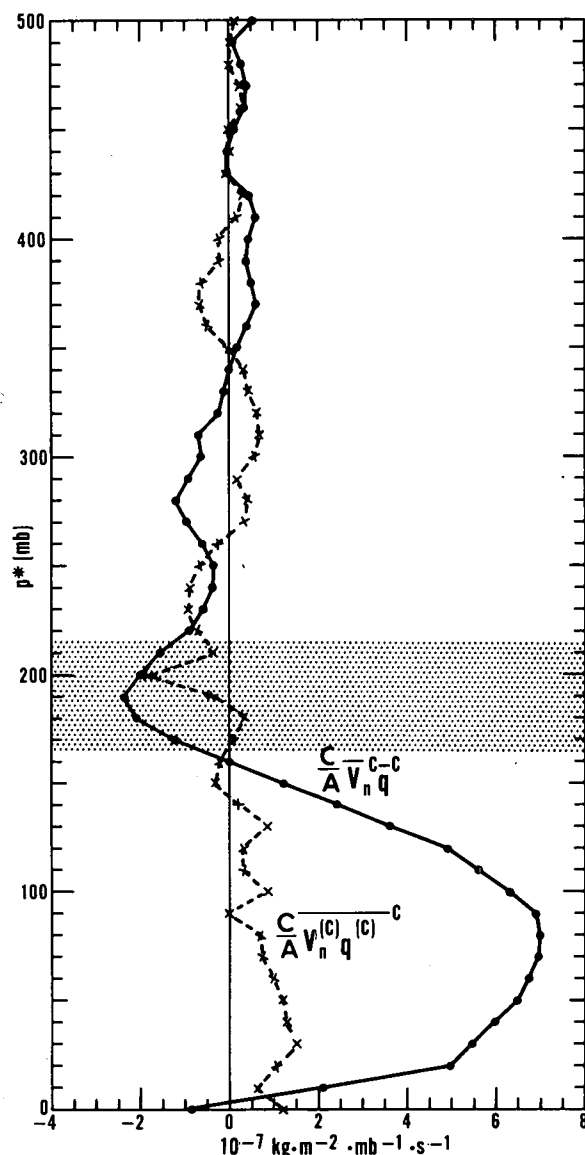


FIGURE 5.—Vertical profiles of $(C/A) (\bar{V}_n^C \bar{q}^C)$, the mean divergence term, and $(C/A) (\bar{V}_n^{(C)} \bar{q}^{(C)})$, the horizontal advection term, in the water vapor budget. The shaded area is the same as in figure 4.

at the surface with a value equal to the evaporation rate and proceeding upward by adding incremental divergence contributions for each layer. This profile, together with profiles of the grid-scale vertical flux and the sum of the two, which represents the total vertical flux, is shown in figure 6. The computations show a rapid decrease in the upward subgrid-scale flux through the trade inversion layer, but the flux does not drop to 10 percent of the surface value until the 300-mb p^* level is reached.

Computations by Augstein et al. (1973), based on data obtained during an undisturbed period of the Atlantic Tradewind Experiment (ATEX), indicate little subgrid-scale water vapor transfer through the top of the inversion. In later studies, we shall attempt to determine whether or not the computed subgrid-scale transfer above $p^*=200$ mb occurred primarily when the trade inversion was unusually weak or displaced from its usual height.

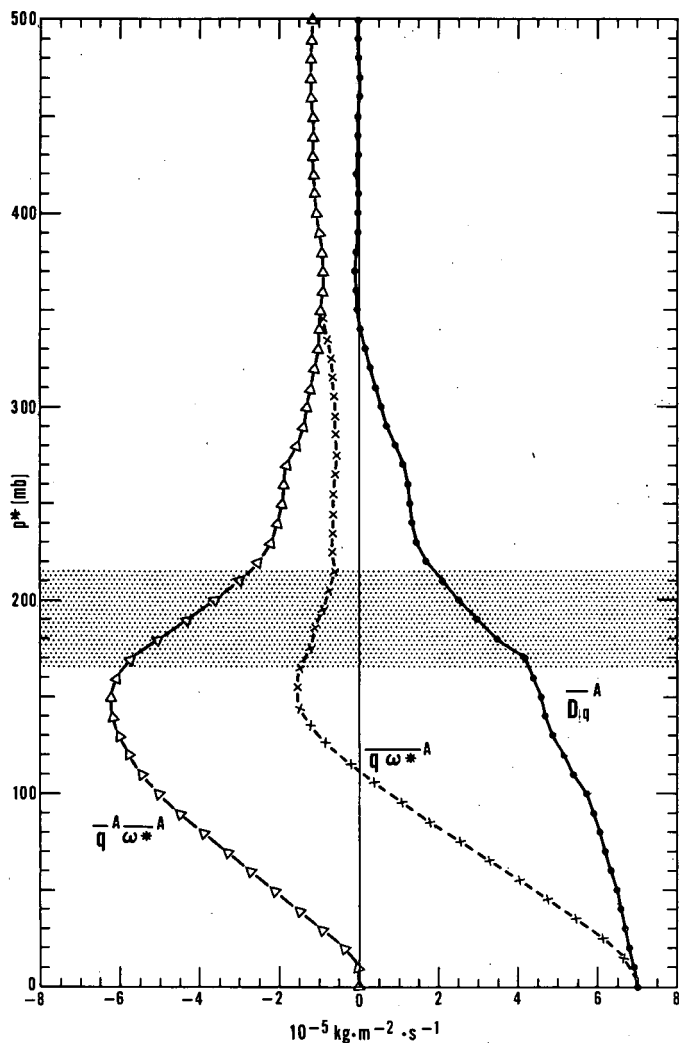


FIGURE 6.—Vertical profiles of $\overline{q\omega^*}^A$, the vertical water vapor flux, $\overline{q\omega^*}^A$, the part due to grid-scale vertical motion, and $\overline{D_q}^A$, the part due to subgrid-scale vertical motion. The shaded area is the same as in figure 4.

The net upward vertical flux (i.e., the sum of the grid-scale and subgrid-scale fluxes) shows a rapid decrease in the first 100 mb, reaching zero around 110 mb. The calculations indicate a net downward flux of water vapor in the upper portions of the cloud layer, with maximum downward transport near the base of the inversion. Above the inversion, we find weak net downward transport.

As pointed out by Riehl et al. (1951), the water balance of the trade inversion is largely maintained by opposite contributions: the downward advection of dry air by the grid-scale flow and the convergence of the upward subgrid-scale moisture transport. This is well illustrated by the profiles of the two vertical flux divergence terms shown in figure 7, offering quite encouraging evidence that reasonable profiles of these quantities may be obtained directly from the basic data.

The heat budget analysis, to be discussed later, suggests that the abrupt increase in grid-scale vertical flux divergence at the base of the trade inversion may be accounted for, in part, by the change from a condensa-

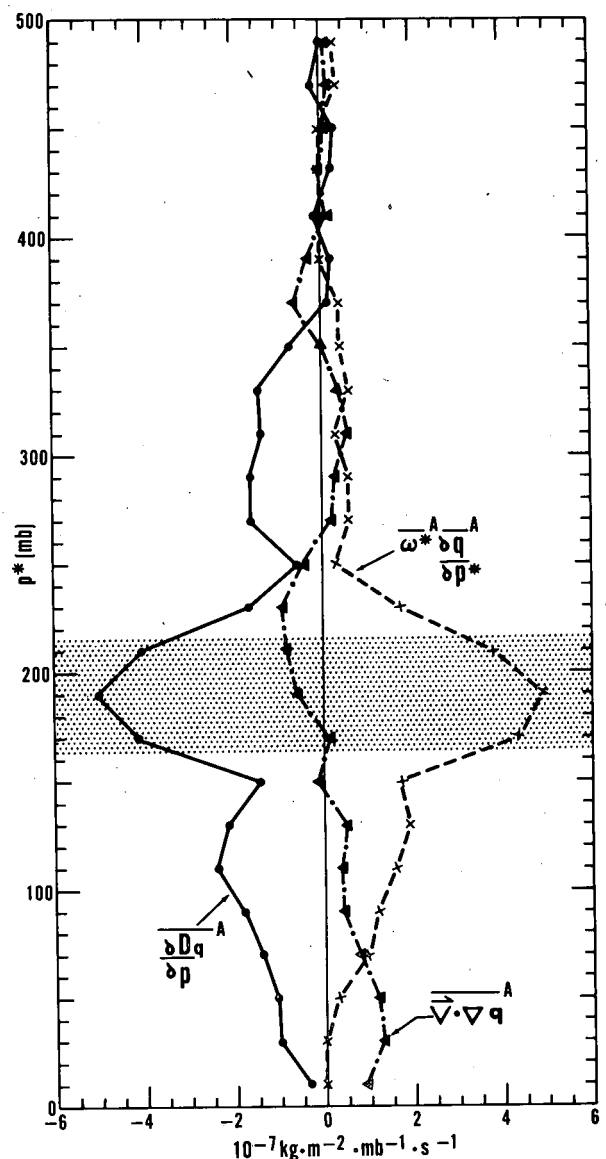


FIGURE 7.—Vertical profiles of $\overline{\nabla \cdot \nabla q}^A$, the horizontal advection of water vapor, $\overline{\omega^* \frac{\partial q}{\partial p}}^A$, the vertical advection, and $\overline{\frac{\partial D_q}{\partial p}}^A$, the vertical subgrid-scale vapor flux divergence. The shaded area is the same as in figure 4.

tion water vapor sink in the cumulus layer to an evaporative source in the trade inversion layer. This change would require an increase in the vertical eddy flux convergence between 60 and 150 mb and a decrease between 150 and 250 mb, resulting in a smoother profile.

7. MOMENTUM BALANCE

For convenience, the momentum budget is computed in a right-handed normal coordinate system, with the positive x axis (positive U component) pointing in the direction of the mean surface wind vector. This requires a clockwise rotation of 174° from the geographical coordinate system, since the mean surface wind direction was 84° . To compute the stress, we must know the value of each stress component at some point on the profile. The following assumptions normally applied in geo-

strophic departure computations (Charnock et al. 1956) have been made:

$$(\tau_y)_0 = 0$$

and

$$(\tau_x)_{80} = 0.$$

In other words, it is assumed that the surface stress vector is parallel to the mean surface wind and that the x component of the stress vanishes at the low-level U maximum. (See fig. 2.) The assumption of a surface stress vector parallel to the 5-day time- and space-averaged surface wind is open to question. As a check, the components of the vector $V|V|$ were computed for all observations during the period, then averaged. The direction of this vector represents an estimate of the direction of the mean surface stress vector, provided the drag coefficient is approximately constant over the range of conditions existing during the period. The computed direction was 83° , a difference of only 1° from that of the mean surface wind.

The assumption of a vanishing stress component at the low-level wind maximum has generally been applied in geostrophic departure computations for the Tropics (Charnock et al. 1956, Janota 1971, Estoque 1971). As noted by Priestley (1959, p. 37), there are few data for either verifying or disproving this assumption. It certainly becomes less secure when applied to time-space averaged wind profiles. On the other hand, the low-level U maximum is a persistent feature on the individual soundings, and its mean height at the four ships varied by only 10 mb.

The accurate measurement of the surface pressure gradient constitutes a major problem in momentum balance computations. Initial computations for the period under study indicated a bias in the measured pressure gradient, detectable as a bias in the computed frictional force that increased with height in proportion to the increase in specific volume.

The requirement for measuring the x component of the surface pressure gradient is removed, if the value of the x stress component is known at a second point on the profile. For instance, an assumption of vanishing stress at a second U extremum can be made, but none exists in the mean U profile for this period. Since the stress in the midtroposphere during undisturbed periods is likely to be quite small, the condition $(\tau_x)_{500} = 0$ was applied.

It is unnecessary to compute the y component of the stress to obtain an estimate of the surface stress, although it is required for a complete evaluation of the stress profile. On the other hand, since the pressure gradient enters into the computation of the kinetic energy balance, it is desirable to compute a correction to both the y component and the x component of the pressure gradient. Unlike the U profile, however, which consistently exhibited an extremum near $p^* = 80$ mb, the height of the V -profile extremum was highly variable from day to day and from ship to ship. To properly apply the condition of vanishing stress at a V extremum, one should perform computations over individual periods and subareas for which the V

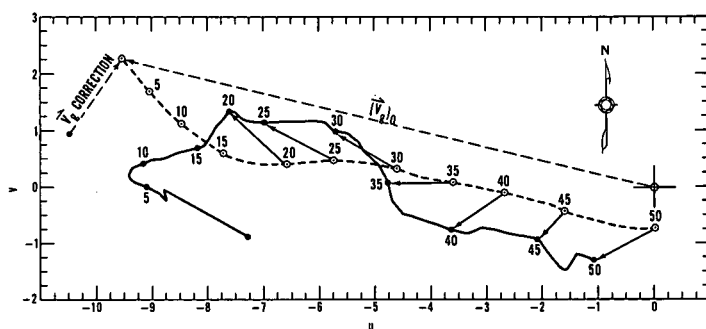


FIGURE 8.—Mean wind hodograph (solid curve) and mean geostrophic wind hodograph (dashed curve). Altitudes indicated at p^* intervals of 50 mb in tens of mb. Westerly and southerly wind components (m/s) are u and v , respectively.

extremum does not vary appreciably with height. Nevertheless, in these trial computations, we applied this condition at the level of the weak extremum of the mean V profile, which was located at $p^* = 220$ mb. Tests were also run with the condition $(\tau_y)_{500} = 0$. These resulted in only minor changes in the magnitude of the computed pressure gradient correction.

The correction in both pressure gradient components amounted to approximately 0.25 mb/500 km. This results in a correction of the geostrophic wind of 1.7 m/s at the surface, increasing to 2.8 m/s at $p^* = 500$ mb and directed from the southwest.

Actual and geostrophic wind hodographs are shown in figure 8. A thermal wind shear is evident throughout the entire geostrophic hodograph, the most rapid changes in direction occurring through the trade inversion. The hodograph for the actual wind shows greater irregularity, which may be due to inadequate editing of noisy azimuth angle measurements during the A_0 data reduction process particularly in the first 30 mb. Improvement is expected in the final A process.

The clockwise frictional turning of the wind in the planetary boundary layer is partly offset by the thermal wind shear. Thus, between the surface and $p^* = 150$ mb where the actual and geostrophic winds are approximately equal, the actual wind turns 12° clockwise while the geostrophic wind turns 8° counterclockwise.

The computations indicate an ageostrophic wind component above the planetary boundary layer, the magnitude of which is generally between 0.5 and 1.5 m/s. Between 160 and 330 mb, the computations show the actual wind to be supergeostrophic and blowing toward high pressure. This layer corresponds very closely with the layer of mean convergence (fig. 4). Above 330 mb, the winds are also supergeostrophic but directed toward low pressure. This layer corresponds to a layer of divergence on the mean profile.

Figure 9 shows the profiles of the individual terms in the x momentum balance. Here, the acceleration term is balanced against forces per unit mass so that the sign of each term is that of its contribution to the acceleration in the direction of the mean surface wind. The following features are noteworthy:

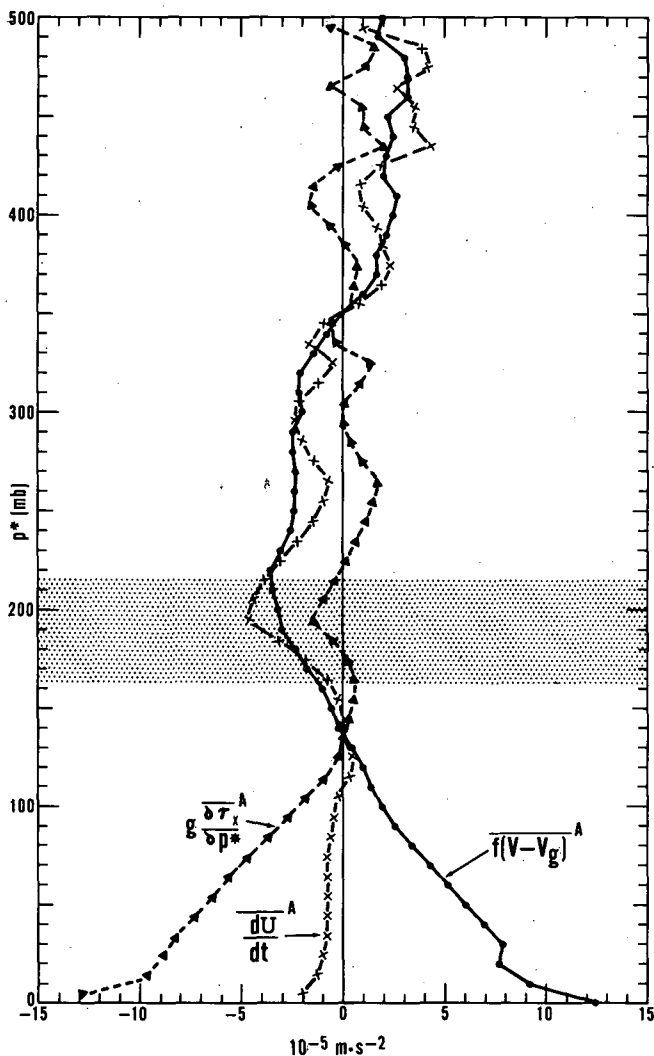


FIGURE 9.—Vertical profiles of $\overline{dU/dt}^A$, total acceleration, $\overline{f(V-V_g)}^A$, the excess of Coriolis over pressure gradient force per unit mass, and $\overline{g(\partial\tau_x/\partial p^*)}^A$, the frictional force in the direction of the mean surface wind. The shaded area is the same as in figure 4.

1. The computed x component of frictional force decreases from a maximum at the surface to zero around 130 mb and remains small above this level. One might, therefore, estimate the top of the friction layer at around 130 mb, or approximately 1300 m. Recall that the subgrid-scale vertical flux of water vapor is still quite large at this level (fig. 6).

2. The acceleration, dU/dt , is relatively small in the friction layer. This term is assumed to be zero in the geostrophic departure technique of computing the surface stress, and our results support that assumption.

3. Computed variations in the frictional force above the planetary boundary layer are small and of questionable validity. In the friction layer, the balance is essentially between the frictional force and the geostrophic departure term, while, above the friction layer, there is approximate balance between the acceleration and the geostrophic departure term. For example, note that the acceleration and geostrophic departure terms are both negative and roughly equal between 140 and 350 mb, while above this level both become positive.

Figure 10 shows a comparison of the computed profiles of $-\tau_x$ and the grid-scale vertical transfer. The computed surface stress is $0.065 \text{ N}\cdot\text{m}^{-2}$. The "surface" wind obser-

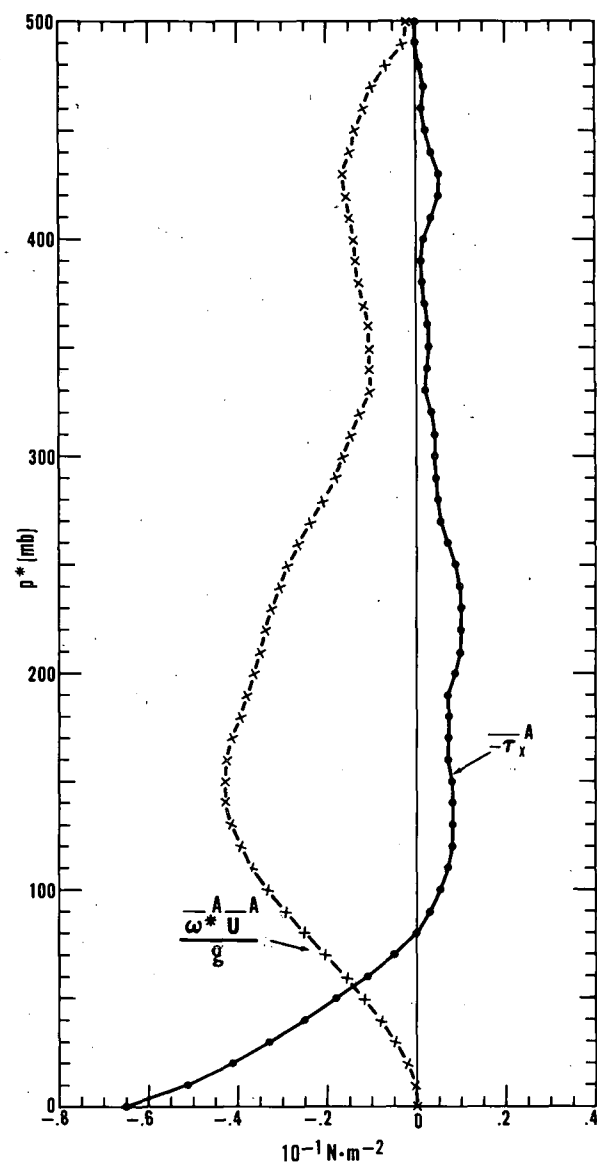


FIGURE 10.—Vertical profiles of $(\overline{\omega^{*A}U^A})/g$, and $-\overline{\tau_x^A}$, the vertical flux of x -component momentum (in the direction of the mean surface wind) due to grid-scale motions and to subgrid-scale vertical motions, respectively.

vations used in this study were obtained from masthead anemometers, approximately 27 m above the sea surface on the *Oceanographer* and *Discoverer* and approximately 22 m above the sea surface on the *Mt. Mitchell* and *Rainier*. Using these winds³ and the computed surface stress, we obtained a drag coefficient of approximately 1.0×10^{-3} .

8. MECHANICAL ENERGY BALANCE

The balance equation for grid-scale kinetic energy is obtained by multiplying the component momentum equations by the respective wind components and adding. The term $-gV\cdot\partial\tau/\partial p^*$ in this equation represents the kinetic

³ Preliminary comparisons of these winds with those measured simultaneously by anemometers mounted on a boom projecting from the bow of each ship indicate that the masthead wind speeds have a negative bias, resulting in an overestimate of the drag coefficient.

TABLE 3.—Kinetic energy balance ($W \cdot m^{-2}$)

Term	Layer (mb)		
	0-150	150-500	0-500
(a) Generation- $(\mathbf{V} \cdot \nabla \phi + \alpha \mathbf{V} \cdot \nabla p_0)$	0.71	-0.50	0.20
(b) Substantial derivative dK/dt	-.05	-.57	-.62
Frictional loss (a) - (b)	0.76	0.07	0.82

energy drained from the grid-scale motion by subgrid-scale frictional effects. It is evaluated in the computations as a residual, the difference between the generation term, $-(\mathbf{V} \cdot \nabla \phi + \alpha \mathbf{V} \cdot \nabla p_0)$, and the substantial derivative, dK/dt .

Profiles of the frictional loss and total derivative terms are shown in figure 11. In the lower 500 mb of the atmosphere, the frictional loss of grid-scale kinetic energy occurs primarily in the planetary boundary layer, as would be expected. Values above $p^*=130$ mb are erratic and small. Table 3 summarizes the values of the three terms of the budget equation for the lowest 150 mb and for the remainder of the column.

Generation and frictional loss terms approximately balance in the lowest 150 mb. Above the boundary layer, however, the balance is primarily between the generation term, which is negative, and the substantial derivative. In other words, the air passing through this upper layer during the 5-day period showed an average decrease in grid-scale kinetic energy, primarily the result of an average ageostrophic wind component toward higher pressure.

As seen from table 3, the computed frictional loss of grid-scale kinetic energy within the planetary boundary layer is approximately $0.8 W \cdot m^{-2}$. For the remainder of the column, the computations show very small losses.

9. HEAT (ENTHALPY) BALANCE

Based solely on rawinsonde data, a heat balance computation can be made that will yield, as a residual, the total input of heat to the column. A high degree of accuracy is required if one is to proceed to the next step, that of obtaining a satisfactory estimate of the sensible heat flux from the sea surface; and in addition, one must accurately evaluate the cooling of the column by radiation and the heating of the column due to condensation. To proceed a step farther to the computation of the profile of vertical subgrid-scale heat flux, one must also obtain accurate estimates of the vertical distribution of the heat sources.

Although the initial heat budget computations have been encouraging, they must be considered as tentative, pending the final estimates of radiative cooling being developed by Cox (1971) and the results obtained with the A rawinsonde data.

Profiles of computed diabatic heating, $(dH/dt) - \alpha \omega^A$, and radiative cooling are shown in figure 12. The difference be-

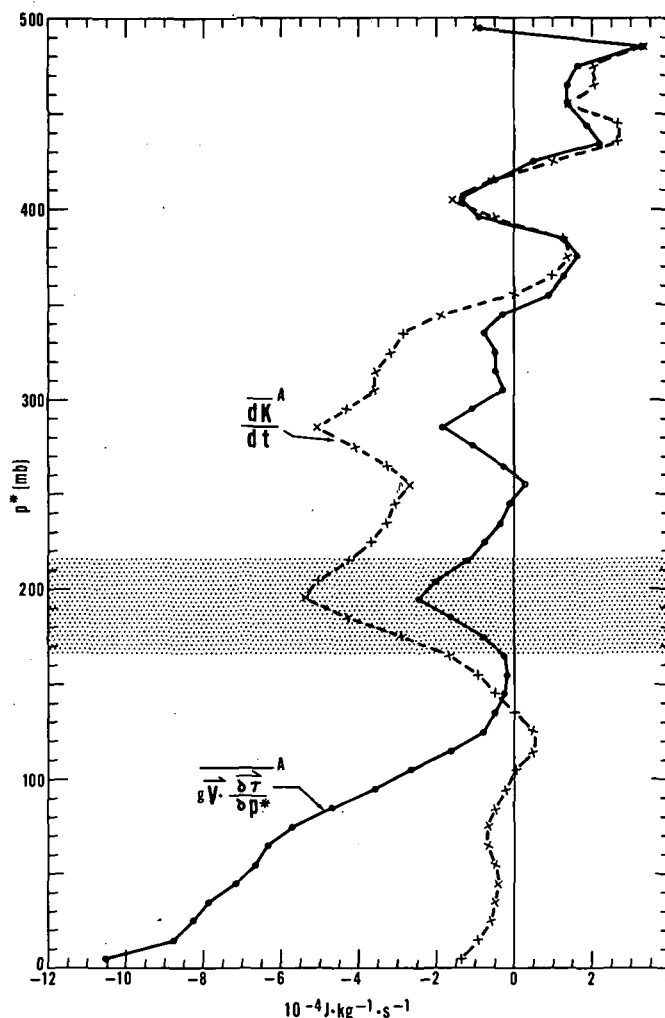


FIGURE 11.—Vertical profiles of $\overline{dK/dt}^A$, the substantial derivative of grid-scale kinetic energy, and $\overline{gV \cdot \partial \tau / \partial p^*}^A$, the rate of change of grid-scale kinetic energy due to subgrid-scale processes. The shaded area is the same as in figure 4.

tween the two curves represents the heating that must be accounted for by subgrid-scale eddy heat flux convergence and condensation heating. The computed, non-radiative, diabatic heating for the column as a whole amounts to $42 \times 10^4 \text{ cal} \cdot m^{-2} \cdot \text{day}^{-1}$. Of this amount, condensation heating accounts for $12 \times 10^4 \text{ cal} \cdot m^{-2} \cdot \text{day}^{-1}$ (0.2 mm/day precipitation), leaving $30 \times 10^4 \text{ cal} \cdot m^{-2} \cdot \text{day}^{-1}$ to be accounted for by heat flux from the ocean if, as is assumed, the subgrid-scale heat flux through the top of the box is negligible. Since evaporation during the period is computed to be 6.0 mm/day, a Bowen ratio of approximately 0.1 is obtained from the atmospheric budget computations.

The diabatic heating not accounted for by radiative processes is represented by the area between the dashed curve and the solid curve on figure 12. The computations show a significant vertical variation in this quantity. Specifically, the layer $p^*=0-150$ mb exhibits a total nonradiative diabatic heating of approximately $82 \times 10^4 \text{ cal} \cdot m^{-2} \cdot \text{day}^{-1}$, while the layer between 150 and 250 mb, which includes the trade inversion, exhibits a cooling of

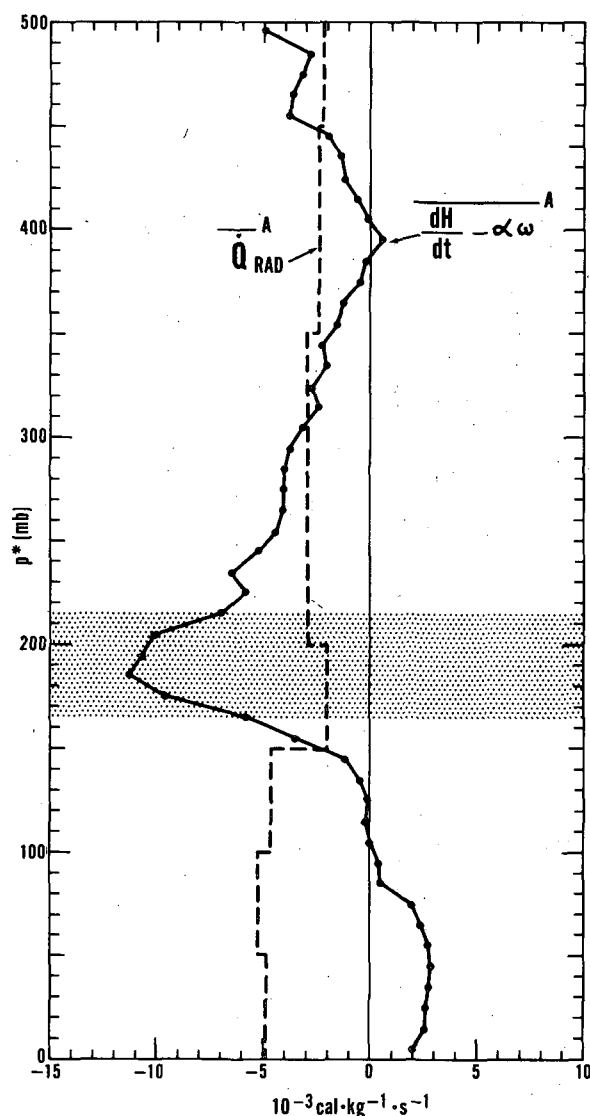


FIGURE 12.—Vertical profiles of $(dH/dt) - \alpha\omega^A$, the net diabatic heating, and \bar{Q}_{RAD}^A , the net radiative heating. The shaded area is the same as in figure 4.

approximately $45 \times 10^4 \text{ cal} \cdot \text{m}^{-2} \cdot \text{day}^{-1}$. Within the framework of this study, the computed variations of non-radiative diabatic heating above $p^* = 250 \text{ mb}$ are probably not significant.

In the subcloud layer ($p^* < 60 \text{ mb}$), there is undoubtedly an eddy flux of heat from below and from above, since it is a region of minimum potential temperature. The gain of heat in the cumulus layer and loss from the trade inversion may merely reflect the redistribution of heat by eddy diffusion, but it may also include a contribution from the vertical separation of preferred condensation and evaporation regions.

If due entirely to evaporation, the observed cooling in the trade inversion layer would require an upward liquid water flux of about $1 \times 10^{-5} \text{ kg} \cdot \text{m}^{-2} \cdot \text{s}^{-1}$ through the 150-mb p^* surface; that is, only 20 percent of the eddy water vapor flux shown at that level in figure 6. The maximum

TABLE 4.—Sea-air fluxes from atmospheric budgets, June 22–26, 1969

	5-day mean	Standard deviation	Standard error
Water vapor (mm/day)	6.0	5.3	± 0.6
Latent heat ($\text{cal} \cdot \text{m}^{-2} \cdot \text{day}^{-1}$)	349×10^4	308×10^4	$\pm 35 \times 10^4$
Sensible heat ($\text{cal} \cdot \text{m}^{-2} \cdot \text{day}^{-1}$)	30×10^4	260×10^4	$\pm 30 \times 10^4$
Momentum ($\text{N} \cdot \text{m}^{-2}$)	-0.065	0.090	± 0.010

heat sink, about $10^{-2} \text{ cal} \cdot \text{kg}^{-1} \cdot \text{s}^{-1}$ observed near $p^* = 200 \text{ mb}$ coincides with the maximum in the vertical advective flux divergence of water vapor shown in figure 7 and would require only about one-third the observed vapor flux divergence. The water vapor sink required to balance the heat source between 60 and 150 mb is similarly compatible with the water vapor eddy flux and flux divergence profiles, being smaller in magnitude than the values derived from the residual of the water vapor budget in this layer.

The above explanation of the heat flux divergence profile is, thus, plausible in terms of consistency between the heat and water vapor budgets. An interesting implication is that a measurable part of the cooling and moistening required to convert sinking trade inversion air into subinversion air may be accomplished by the evaporation of cumulus tops in the inversion layer. However, the vertical gradients of temperature and humidity through the inversion layer are such that the observed flux divergences may be explainable, at least qualitatively, on the basis of an upward decrease in the eddy diffusivities.

10. SUMMARY AND CONCLUSIONS

Vertical profiles of residuals of the budget equations, after accounting for source terms and integrating with reasonable boundary conditions, yield the values for the 5-day mean surface fluxes shown in table 4. This table also shows the standard deviations of the 77 values computed for the individual $1\frac{1}{2}$ -hr observation times after removal of the variance due to the local time derivative (storage) terms; these errors largely cancel out over the averaging period. An estimate of the standard error of each 5-day mean was obtained by dividing these standard deviations by the square root of 77, which is equivalent to assuming that all the variance of the $1\frac{1}{2}$ -hr values is due to random, uncorrelated errors. To the extent that the observed variance includes real meteorological variations, whether serially correlated or not, this error estimate is too high. To the extent that the errors in the observations and in the derived quantities are serially correlated, on the other hand (as a result, e.g., of the filtering process), these estimates of standard error may be low, since the degrees of freedom would have been overestimated.

The evaporation rate, 6 mm/day, is about 20 percent higher than that expected from the climatological estimates by Jacobs (1951) and Budyko (1963). The standard error in the 5-day average evaporation rate is estimated at 10 percent by the method described above. Independent estimates for this same time period obtained by analysis of the ocean heat budget (Delnore 1972) and by applying the bulk aerodynamic method to surface data from the five fixed ships are 5.1 and 5.6 mm/day, respectively. It is possible that the method of eliminating the diurnal variation of the radiosonde humidities has introduced a slight positive bias in all the terms of the water vapor budget. However, the values may also show a negative bias of around 5–10 percent, due to the humidity error arising from the thermal lag of the hygistor. A correction for this error will be applied in future analyses.

Boundary-layer measurements are not available for the period analyzed here. A rather comprehensive survey of the BOMEX square on June 29, 1969, by a NOAA DC-6 aircraft equipped with turbulence sensors gave an average vertical eddy flux of water vapor, at 150 m and below, requiring an evaporation rate of 6.1 mm/day. During the first 2 weeks of May, turbulent flux measurements were made aboard the Navy's Floating Laboratory Instrument Platform (FLIP), as well as by aircraft. Results obtained by several different methods of measurement during that period also ranged from about 5 to 6 mm/day. These measurements also agree in showing variations from less than 4 to more than 8 mm/day over periods of hours and days. Thus, it seems likely that a large fraction of the variance of evaporation rate shown in table 4 is real and the errors are sufficiently small for measurement of day-to-day changes to be useful for testing parameterization and simulation models.

The Bowen ratio turned out to be 0.1, well within the range of previous estimates. The reasonableness of the computed sea-air fluxes and their agreement with independent measurements, as well as the physically plausible interrelationships of the vertical profiles of the subgrid-scale fluxes, should encourage the use of these results in developing eddy diffusion coefficients for synoptic scale numerical modeling.

The frictional boundary layer was surprisingly well defined, although the boundary layer depth differed for momentum, water vapor, and heat. The frictional force approached zero at $p^* = 130$ mb, and the wind was most nearly geostrophic in the layer between 130 and 160 mb, below the base of the trade inversion. There was an Ekman spiral with the maximum wind speed at 80 mb. The actual and geostrophic winds showed a directional difference of 20° at the surface. However, because of an 8° backing of the geostrophic wind, the actual wind turned clockwise by only 12° through the boundary layer.

Because the acceleration was negligible within the boundary layer, the geostrophic departure method should give an excellent measure of the surface stress if sufficiently accurate horizontal pressure gradient measurements were available. Unfortunately, the observed sea-level pressure

differences across the array appear to be in error by about 0.25 mb, which, if not corrected, would cause an intolerable error in the computed stress. The "correct" pressure gradient can be estimated by making reasonable assumptions about the relationship of the stress to the wind profiles.

The boundary layers for heat and water vapor, defined as the layer within which subgrid-scale vertical transfers are important, were thicker than for momentum, extending through the trade inversion to a p^* level of 250 to 300 mb. Within the upper portion of this boundary layer, the heat flux was apparently downward, although there was a net upward flux from the sea to the air. A major part of this apparent downward flux of sensible heat may actually have been accomplished by latent heat release in the lower part of the cumulus layer and evaporative cooling in the trade inversion layer.

As expected, the kinetic energy gain and loss terms are more than two orders of magnitude smaller than the latent heat budget terms. Nevertheless, the profiles of the individual terms appear to be realistic, showing an approximate balance in the boundary layer between production and loss due to subgrid-scale frictional effects. Above the boundary layer, the winds were, on the average, supergeostrophic and decelerating, with a net conversion of kinetic to potential energy.

In this preliminary analysis of rawinsonde data only, we have demonstrated encouraging progress toward attaining the goal of $\pm 25 \times 10^4 \text{ cal} \cdot \text{m}^{-2} \cdot \text{day}^{-1}$ for accuracy of the 24-hr average sea-air energy flux (Holland 1970). Future incorporation of aircraft and dropsonde data and more refined editing and correction of the rawinsonde data offer possibilities for further improvements.

ACKNOWLEDGMENTS

We are grateful to Stephen Cox for providing us with the values of radiative cooling used in the computations and to Scott Williams and Thomas Carpenter for their help in data processing and analysis. We also thank May Laughrun for her assistance in editing the manuscript.

REFERENCES

- Augstein, A., Riehl, H., Ostapoff, F., and Wagner, V., "Mass and Energy Transports in an Undisturbed Atlantic Trade Wind Flow," *Monthly Weather Review*, Vol. 101, No. 2, Feb. 1973, (in press).
- BOMAP Office, *BOMEX Field Observations and Basic Data Inventory*, National Oceanic and Atmospheric Administration, U.S. Department of Commerce, Rockville, Md., 1971, 428 pp.
- Budyko, M. I., Editor, *Atlas Teplovogo Balansa Zemnogo Shara* (Atlas of the Heat Balance of the Globe), U.S.S.R. Academy of Sciences, Moscow, 1963, 69 pp.
- Charnock, H., Francis, J. R. D., and Sheppard, P. A., "An Investigation of Wind Structure in the Trades: Anegada 1953," *Philosophical Transactions of the Royal Society of London*, Ser. A, Vol. 249, No. 963, England, Oct. 18, 1956, pp. 179–234.
- Cox, Stephen, Department of Atmospheric Science, Colorado State University, Fort Collins, Colo., Dec. 1971 (personal communication).
- Davidson, Ben, "The Barbados Oceanographic and Meteorological Experiment," *Bulletin of the American Meteorological Society*, Vol. 49, No. 9, Sept. 1968, pp. 928–934.

- Delnore, V. E., "The Diurnal Variation of the Temperature Structure and Some Aspects of the Heat Transfer at the BOMEX Fixed Stations," *Journal of Physical Oceanography*, Vol. 3, No. 2, July 1972, pp. 239-247.
- Estoque, Mariano A., "The Planetary Boundary Layer Wind Over Christmas Island," *Monthly Weather Review*, Vol. 99, No. 3, Mar. 1971, pp. 193-201.
- Holland, Joshua Z., "Preliminary Report on the BOMEX Sea-Air Interaction Program," *Bulletin of the American Meteorological Society*, Vol. 51, No. 9, Sept. 1970, pp. 809-820.
- Holland, Joshua Z., "Interim Report on Results From the BOMEX Core Experiment," *BOMEX Bulletin* No. 10, The BOMAP Office, National Oceanic and Atmospheric Administration, U.S. Department of Commerce, Rockville, Md., June 1971, pp. 31-43.
- Holland, Joshua Z., "Comparative Evaluation of Some BOMEX Measurements of Sea Surface Evaporation, Energy Flux and Stress," *Journal of Physical Oceanography*, Vol. 2, No. 4, Oct. 1972, pp. 476-486.
- Jacobs, Woodrow Cooper, "The Energy Exchange Between Sea and Atmosphere and Some of Its Consequences," *Bulletin of Scripps Institution of Oceanography*, Vol. 6, No. 2, University of California, La Jolla, 1951, 122 pp.
- Janota, P., "An Empirical Study of the Planetary Boundary Layer in the Vicinity of the Intertropical Convergence Zone," Ph. D. thesis, Massachusetts Institute of Technology, Cambridge, 1971, 278 pp.
- Malkus, Joanne S., "Large-Scale Interactions," *The Sea*, Vol. 1: Physical Oceanography, Interscience Publishers, New York, N.Y., 1962, 864 pp. (See pp. 88-294.)
- Priestley, Charles Henry Brian, *Turbulent Transfer in the Lower Atmosphere*, University of Chicago Press, Ill., 1959, 130 pp. (See pp. 33-38.)
- Rasmusson, Eugene M., "Mass, Momentum, and Energy Budget Equations for BOMAP Computations," *NOAA Technical Memorandum ERL BOMAP-3*, The BOMAP Office, National Oceanic and Atmospheric Administration, U.S. Department of Commerce, Rockville, Md., Jan. 1971a, 32 pp.
- Rasmusson, Eugene M., "BOMEX Atmospheric Mass and Energy Budgets: Preliminary Results," *BOMEX Bulletin* No. 10, The BOMAP Office, National Oceanic and Atmospheric Administration, U.S. Department of Commerce, Rockville, Md., June 1971b, pp. 44-50.
- Riehl, Herbert, Yeh, Tu-chang, Malkus, Joanne S., and LaSeur, Noel E., "The North-East Trade of the Pacific Ocean," *Quarterly Journal of the Royal Meteorological Society*, Vol. 77, No. 334, London, England, Oct. 1951, pp. 598-626.
- Teweles, Sidney, "A Spurious Diurnal Variation in Radiosonde Humidity Records," *Bulletin of the American Meteorological Society*, Vol. 51, No. 9, Sept. 1970, pp. 836-840.

[Received May 12, 1972; revised November 20, 1972]

PICTURE OF THE MONTH

High-Altitude Minuteman Exhaust Trail

O. H. DANIEL—*Pqn American Airlines, Cape Kennedy Air Force Station, Fla.*

H. W. BRANDLI and J. ERNST—*Detachment 11, 6th Weather Wing,
Air Weather Service, Patrick Air Force Base, Fla.*

1. INTRODUCTION

Near sunset on Oct. 26, 1970, Thomas Oliver, a meteorologist with the 58th Weather Reconnaissance Squadron, Kirtland Air Force Base, N. Mex., was flying in an RB-57 aircraft above 70,000 ft over California between Edwards and Vandenberg Air Force Bases. The photograph in figure 1 was taken by Oliver at that time. At 1600 LST, a Minuteman solid fuel rocket was launched from Vandenberg. Clearly shown in figure 1 is the rocket's exhaust trail, which Oliver estimated was near 200,000 ft (60 km) and drifting toward the northwest.

2. DISCUSSION

Much information has come from the optical tracking of chemiluminescent trails produced in the upper atmosphere at twilight by the ejection of certain materials from rockets (Craig 1965). Wind data from photos of these trails have not given us much climatological information

on prevailing winds, but such data can show a unique picture of the instantaneous vertical and horizontal distribution of wind at a location (Justus et al. 1971). Numerous observations collected by aufm Kampe et al. (1962) show large vertical wind shears. The chaotic appearance of the Minuteman exhaust trail in figure 1 clearly shows the result of large vertical shears.

What is seen in figure 1 is believed to be predominantly the scattering of light by aluminum oxide particles; any ice crystals have probably dissipated. The Minuteman rocket is a three-stage, solid fuel rocket that burns to an altitude of over 200,000 ft. The exhausts are made up of the following constituents:

CO ₂	2.8%
H	2.0%
H ₂ O	10.7%
N	9.0%
CO	25.8%
HCL	20.2%
ALO	29.5% (5-μm dust particles).

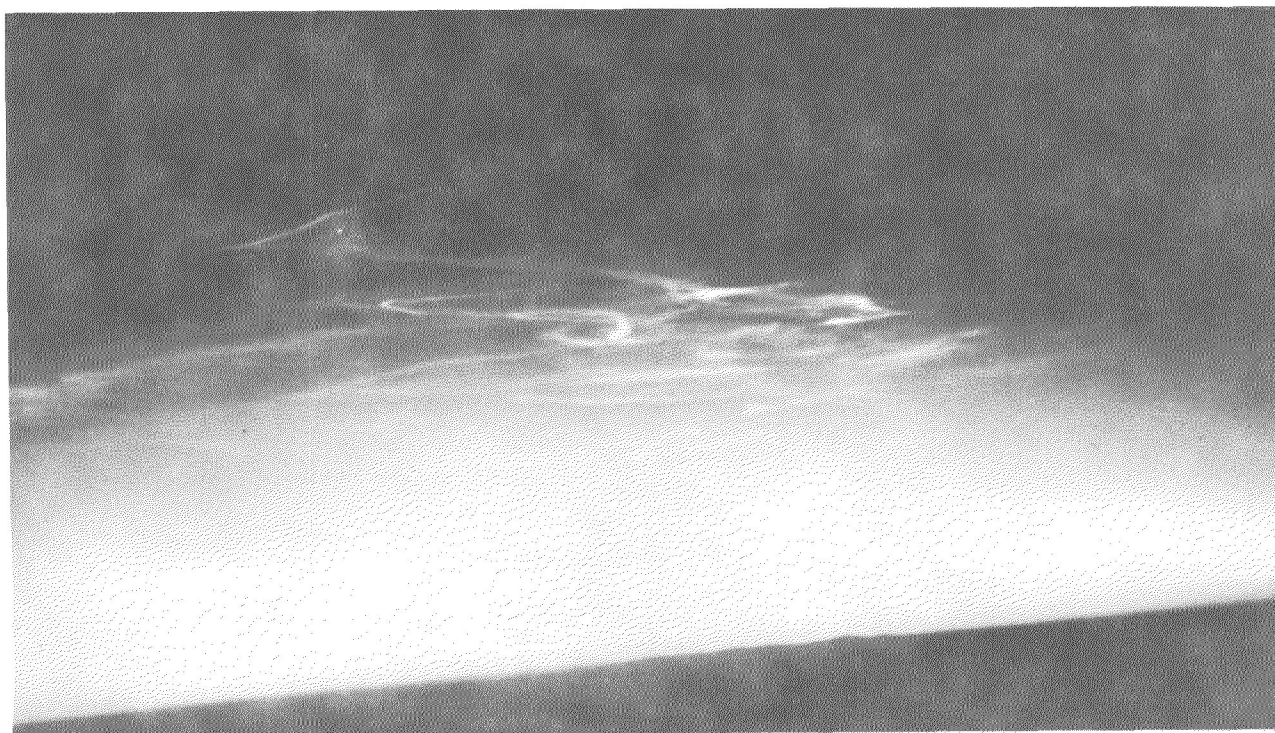


FIGURE 1.—High-altitude Minuteman rocket exhaust trail on Oct. 26, 1970.

Rosenberg (1971) stated that the ALO particles would drift slowly downward from 300,000 ft, and that is what is shown in figure 1. ALO particles above 300,000 ft would initially fall very rapidly and then drift slowly down to about 200,000 ft.

REFERENCES

- aufm Kampe, H. J., Smith, M. E., and Brown, R. M., "Winds between 60 and 110 Kilometers," *Journal of Geophysical Research*, Vol. 67, No. 11, The American Geophysical Union, Washington, D.C., Oct. 1962, pp. 4243-4257.
- Craig, Richard A., *The Upper Atmosphere: Meteorology and Physics*, Academic Press, New York, N.Y., Nov. 1965, 509 pp.
- Justus, Carl G. and Edwards, Howard D., "Winds Observed from July 1968 through November 1970 in the 83 to 216 km Altitude Region," *Final Report AFCRL-71-0311*, Contract No. F19628-68-C-0081, Georgia Institute of Technology, Atlanta, Ga., May 1971, 55 pp.
- Rosenberg, Norman W., Air Force Cambridge Research Laboratories, Cambridge, Mass., Dec. 1971 (personal communication).

[Received September 27, 1971; revised September 26, 1972]